

Effect of Soil Anisotropy on Ground Motion Characteristics

Yuhong Xie ^{1,2}, Zhou Cao ³ and Jian Yu ^{1,2,*}

¹ Department of Geotechnical Engineering, Tongji University, Shanghai 200092, China; 2310070@tongji.edu.cn

² Key Laboratory of Geotechnical and Underground Engineering of Ministry of Education, Tongji University, Shanghai 200092, China

³ Nuclear Power Operations Research Institute, Shanghai 200120, China; caozhou@cnpn.com.cn

* Correspondence: 002yujian@tongji.edu.cn

Abstract: Soil transverse isotropy results in different stiffness characteristics in horizontal and vertical directions. However, the effect is usually neglected in seismic motion analysis. In this study, an equivalent linear anisotropic soil model was established based on the finite element method, and we investigated the impact of anisotropic parameters on ground motion at the site under various seismic wave inputs. It was found that the anisotropic parameters have a more significant effect on seismic waves, with the dominant frequency being closer to the fundamental frequency of the site. As an example, the soil dynamic parameters in Shanghai Yangshan Port were calibrated by a series of bending elements, resonance columns, and cyclic triaxial tests. The influences of anisotropy on the peak ground acceleration (PGA) and response spectrum were studied for Yangshan Port. Additionally, the standard design response spectra considering the soil anisotropy were provided. A comparison reveals that the existing isotropic design response spectrum may lead to dangerous seismic design for the structures at Yangshan port.

Keywords: transverse isotropy; ground motion characteristics; standard design response spectrum



Citation: Xie, Y.; Cao, Z.; Yu, J. Effect of Soil Anisotropy on Ground Motion Characteristics. *Buildings* **2023**, *13*, 3017. <https://doi.org/10.3390/buildings13123017>

Academic Editor: Mengmeng Lu

Received: 11 October 2023

Revised: 29 November 2023

Accepted: 1 December 2023

Published: 3 December 2023



Copyright: © 2023 by the authors. Licensee MDPI, Basel, Switzerland. This article is an open access article distributed under the terms and conditions of the Creative Commons Attribution (CC BY) license (<https://creativecommons.org/licenses/by/4.0/>).

1. Introduction

To improve the seismic design of structures, it is necessary to conduct a site-specific seismic motion analysis to understand the characteristics of ground motion at the site. Earthquakes have resulted in significant economic losses and casualties. Earthquakes have the potential to inflict significant destruction upon various types of structures, encompassing inland buildings [1], hydraulic structures [2], and subterranean constructions [3]. One of the important causes of the structural damage caused by earthquakes is soil amplification. This is illustrated in damage assessments of buildings in the countries of Turkey [4–6], Greece [7], Iran [8], Mexico [9], Korea [10], Pakistan [11], and Nepal [12]. Numerous scholars have extensively researched the seismic resilience of engineering structures [13–16]. The analysis of structures for seismic resistance utilizes a range of methodologies, encompassing response spectrum analysis, the base shear method (quasi-static method), and time history analysis. The response spectrum method is extensively utilized as the predominant seismic analysis approach in engineering practice. The response spectrum is obtained by calibrating ground motion characteristics at the specific site. Consequently, numerous scholars have researched the seismic design of structures based on the seismic motion characteristics at the site [16–18].

Soil dynamic constitutive models can be categorized into total stress models and effective stress models, considering the aspects of stress transmission and inter-particle contact [19]. The effective stress model offers superior capability in addressing the issue of seismic liquefaction [20–22]. Regarding the issue of seismic ground motion response, researchers commonly employ the total stress model for analysis. The total stress models include the elastic–plastic model [23–30], nonlinear model [22,31,32], and equivalent linear model [33]. Traditional elastoplastic models such as the Mohr–Coulomb model [34] and the

Drucker–Prager model [35] can be integrated with the boundary interface theory [25–27], kinematic hardening theory [23,24], and nested yield surface theory [29,30] to account for the effects of cyclic loading. Although the elastoplastic model theory effectively describes the hysteresis characteristics and nonlinearity of soils, its computational complexity and significant workload make it inconvenient for engineering applications. Researchers employ nonlinear models [31,32] based on the Masing criteria to depict the nonlinearity and hysteresis characteristics of soils. While these nonlinear models simplify the workload associated with elastoplastic models, they still entail a certain level of complexity. The linear model offers the advantages of a low workload and low complexity, allowing for the consideration of soil nonlinearity and hysteresis characteristics through the application of an equivalent concept. Hence, the most widely utilized approach at present is the equivalent linear model, which has evolved from linear models. Schnabel [33] initially pioneered the development of the frequency domain equivalent linear model within the SHAKE program. Idriss et al. [36] modified the expression of damping in the SHAKE program and developed the SHAKE91 program. With the development of commercial software, the SHAKE and SHAKE91 programs have been integrated into software such as EERA 1998 and DEEPSOIL v7.0.33. The SHAKE program demonstrates limited proficiency in effectively addressing anisotropic challenges.

Soil anisotropy has aroused great interest in recent years. Zhang et al. [37,38] and Teng [39] investigated the impact of soil anisotropy on excavation-induced effects in excavations. Wei et al. [40], Soe et al. [41], and Zhang et al. [42] investigated the impact of soil anisotropy on tunnel design and construction. Peric et al. [43] and Ai et al. [44,45] investigated the impact of anisotropy on the design of pile foundations. It has been found that there is anisotropy in the soil under small strain conditions. Bentil [46] has delved into the anisotropy of the small-strain shear modulus by conducting bending element experiments. The consideration of soil anisotropy in the seismic response analysis of soil layers has been scarce among scholars, primarily due to the complexities involved in studying anisotropy, seismic loads, and their associated intricacies. Considering the lack of relevant research and to maintain the coherence and rigor of scientific inquiry, this study investigates the impact of anisotropy on the seismic response of the site using a finite element method with an anisotropic time-domain equivalent linear model.

2. Soil Dynamic Characteristics

2.1. Linear Viscoelastic Model

The viscoelastic Kelvin model (a spring connected in parallel with a sticky pot) is used to reflect the hysteresis of the soil under cyclic loading. The stress–strain relationship is described by Equation (1):

$$\tau = G\gamma + \eta_G \dot{\gamma} \quad (1)$$

where G is the shear modulus; τ is the shear stress; γ is the shear strain; and η_G is the shear viscosity coefficient, as given in Equation (2):

$$\eta_G = \frac{2GD}{\omega} \quad (2)$$

where D is the damping ratio and ω is the circular frequency.

2.2. Modulus and Damping Models

The key to the effective linearization method is to determine the relationship between the shear modulus ratio and the damping ratio with the shear strain. Hyperbolic models are widely used to describe nonlinear soil behavior under cyclic loading, such as the Pyke model and the Stokoe model [47]. In this study, the improved Stokoe model is selected to fit the relationship between the shear modulus ratio and shear strain, as given in Equation (3):

$$G_{norm} = \frac{G}{G_{max}} = \frac{1}{1 + (r/r_r)^\alpha} \quad (3)$$

where G_{norm} is the normalized shear modulus, r_r is the reference strain, and α is the fitting parameter; the definition of r_r is different from the Harden–Drnevich model ($r_r = \tau_{max}/G_{max}$).

Zhang et al.'s [48] formula is adopted to describe the relationship between D and G_{norm} as follows:

$$D = K_1 G_{norm}^2 + K_2 G_{norm} + K_3 \quad (4)$$

where K_1 , K_2 , K_3 are the model fitting parameters.

2.3. Effects of Anisotropy

The notation for an anisotropic material used herein is the y -axis (the vertical direction) represents the direction of the anisotropy, and the x, z -plane is the plane of isotropy. The stress–strain increment equation for an anisotropic material can be written as follows (5) [49].

$$\begin{pmatrix} \delta\varepsilon_x \\ \delta\varepsilon_y \\ \delta\varepsilon_z \\ \delta\gamma_{xy} \\ \delta\gamma_{yz} \\ \delta\gamma_{zx} \end{pmatrix} = \begin{bmatrix} \frac{1}{E_h} & -\frac{\nu_{vh}}{E_v} & -\frac{\nu_{hh}}{E_h} & 0 & 0 & 0 \\ -\frac{\nu_{hv}}{E_h} & \frac{1}{E_v} & -\frac{\nu_{hv}}{E_h} & 0 & 0 & 0 \\ -\frac{\nu_{hh}}{E_h} & -\frac{\nu_{vh}}{E_v} & \frac{1}{E_h} & 0 & 0 & 0 \\ 0 & 0 & 0 & \frac{1}{G_{hv}} & 0 & 0 \\ 0 & 0 & 0 & 0 & \frac{1}{G_{vh}} & 0 \\ 0 & 0 & 0 & 0 & 0 & \frac{1}{G_{hh}} \end{bmatrix} \begin{pmatrix} \delta\sigma_x \\ \delta\sigma_y \\ \delta\sigma_z \\ \delta\sigma_{xy} \\ \delta\sigma_{yz} \\ \delta\sigma_{zx} \end{pmatrix} \quad (5)$$

where E_v and E_h are Young's moduli in the vertical and horizontal directions, respectively; ν_{hh} and ν_{vh} are Poisson's ratios for horizontal strains from a horizontal and vertical strain, respectively; ν_{hv} is Poisson's ratio for vertical strains from a horizontal strain; G_{vh} and G_{hv} are the shear moduli in the vertical plane; and G_{hh} is the shear modulus in the horizontal plane.

The anisotropy ratios AR_G and AR_E for the shear modulus and Young's modulus are, respectively, defined as:

$$AR_G = \frac{G_{hh}}{G_{vh}} \quad (6)$$

$$AR_E = \frac{E_h}{E_v} \quad (7)$$

Under the undrained condition, these Poisson's ratios [50] need to satisfy the additional relationships ($\nu_{vh} = 0.5, \nu_{hh} + \nu_{vh} = 1$). Therefore, one can further obtain the following equations [50]:

$$\nu_{hh} = 1 - \nu_{vh} = 1 - AR_E \cdot \nu_{vh} \quad (8)$$

$$\nu_{hv} = \frac{E_h}{E_v} \cdot \nu_{vh} = AR_E \cdot \nu_{vh} \quad (9)$$

$$G_{hh} = \frac{AR_E \cdot E_v}{2(2 - AR_E \cdot \nu_{vh})} \quad (10)$$

$$G_{vh} = G_{hv} = \frac{1}{AR_G} \frac{AR_E \cdot E_v}{2(2 - AR_E \cdot \nu_{vh})} \quad (11)$$

3. Simulation of Time-Domain Equivalent Linear Model for Anisotropic Soil Layers

This study takes the actual recorded seismic waves as input conditions, degenerates the model to isotropy, and compares it with EERA for verification. This study focuses on exploring the ground motion response of anisotropic sites with different sedimentary characteristics (different anisotropic parameters).

3.1. Input Ground Motion and Finite Element Model

In Eurocode 8 [51], sites are classified according to the average shear wave velocity in the upper 30 m thick soil profile. Therefore, the soil layer thickness is selected as 30 m. Also, three seismic waves are chosen: the Ei-Centro Wave, Shanghai Wave, and Kobe Wave. The amplitudes of these seismic waves were adjusted to have a peak acceleration of 0.1 g. Figure 1 illustrates the three seismic waves. As shown in Figure 2, a two-dimensional plane strain soil finite element model is established based on ABAQUS 6.14. The type of the finite element is CPE4, and the estimated size of the mesh is $1\text{ m} \times 1\text{ m}$. The mesh size meets the requirement of less than $1/10$ wavelength. The boundary adopts the infinite element boundary, and seismic waves are input to the base. Therefore, the wave vibrates in the x direction and propagates in the y direction.

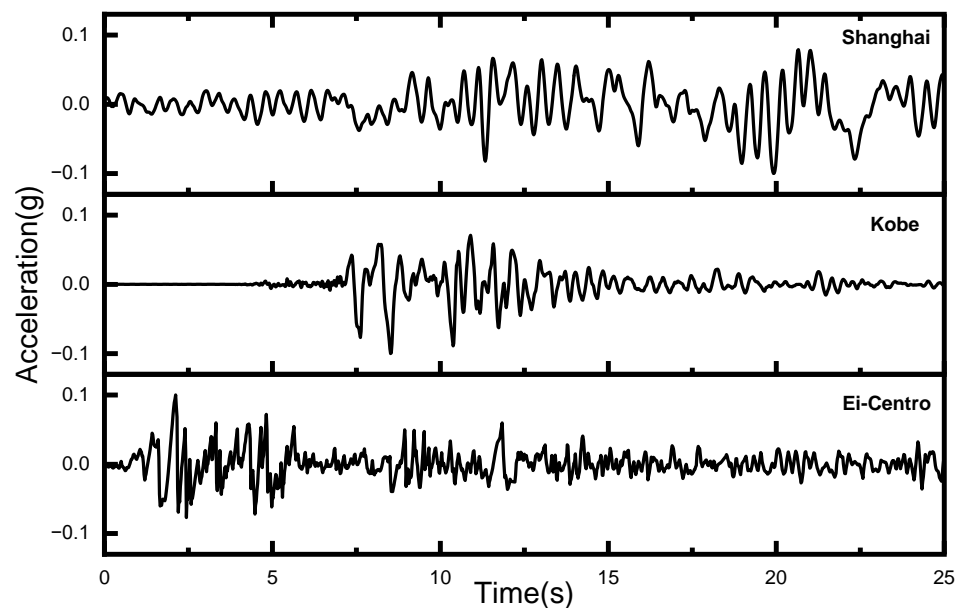


Figure 1. Seismic wave time history curve.

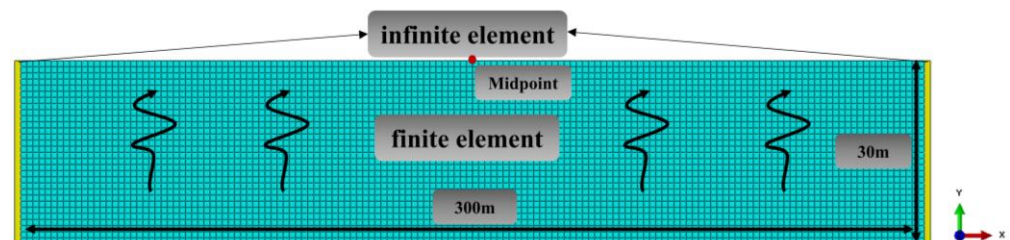


Figure 2. Finite element model.

3.2. Isotropic Soil Layer

This subsection is used to verify the validity of the established finite element method with an anisotropic time-domain equivalent linear model in the isotropic case studies. The shear modulus model chosen here is the Seed–Idriss mode [52], and the damping curve model used is the Idriss mode [36]. Table 1 presents the model parameters. The properties of the soil layers are shown in Table 2.

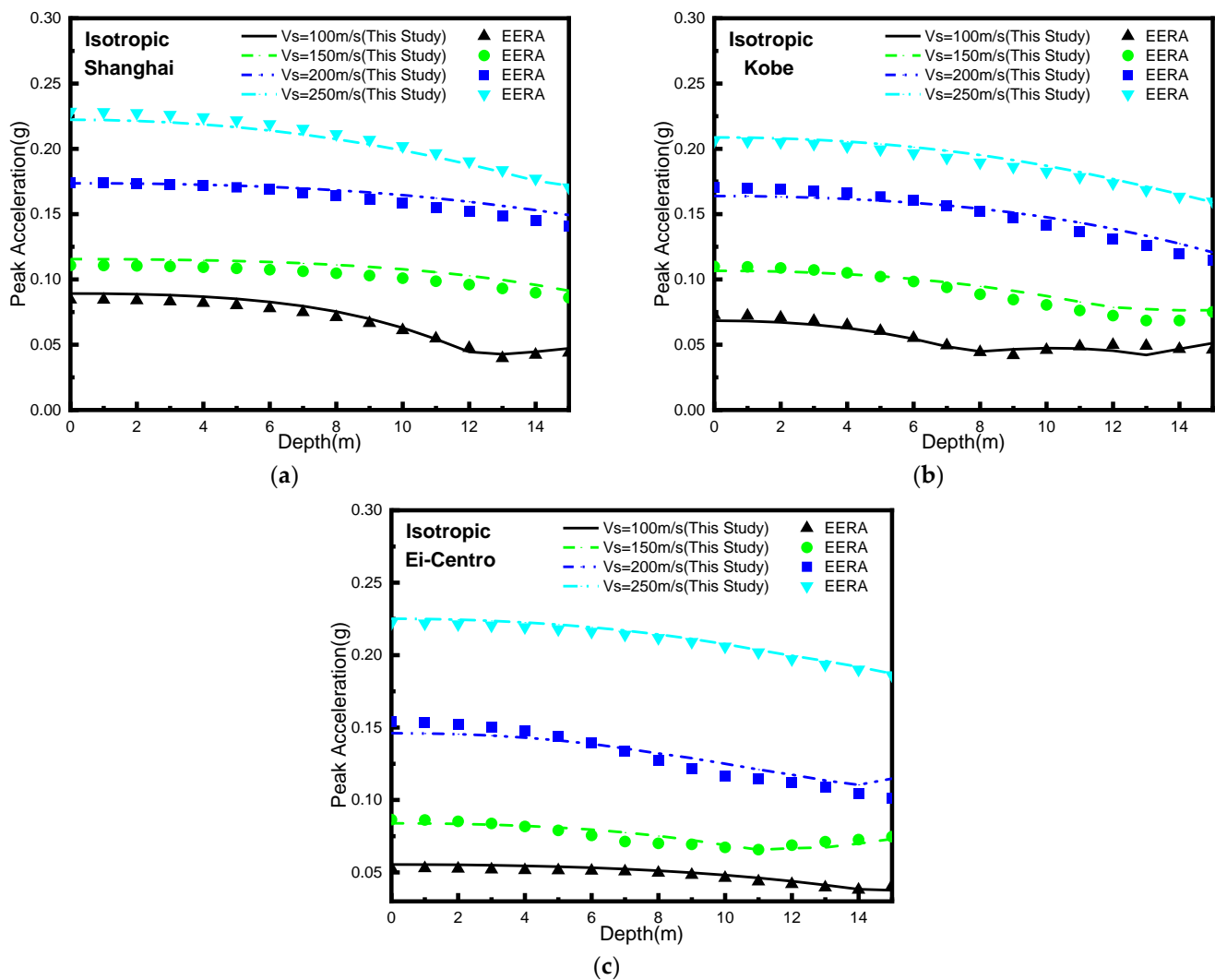
Table 1. Model parameters.

$\gamma_\gamma (10^{-4})$	α	K_1	K_2	K_3
5.87	0.93	0.26	−0.51	0.26

Table 2. Isotropic soil example.

Seismic Wave	Thickness (m)	V_s (m/s)	ρ (g/cm ³)
EI-Centro; Shanghai; Kobe	30	100	2
		150	
		200	
		300	

Figure 3 illustrates the comparison of the peak ground acceleration (PGA) with depth, considering three seismic records, namely the Ei-Centro Wave, Shanghai Wave, and Kobe Wave, along with four soil conditions. They exhibit good agreements with the results obtained from the classical seismic analysis code EERA.

**Figure 3.** Comparison of results for homogeneous soil layer with isotropic: (a) Shanghai; (b) Kobe; (c) Ei-Centro.

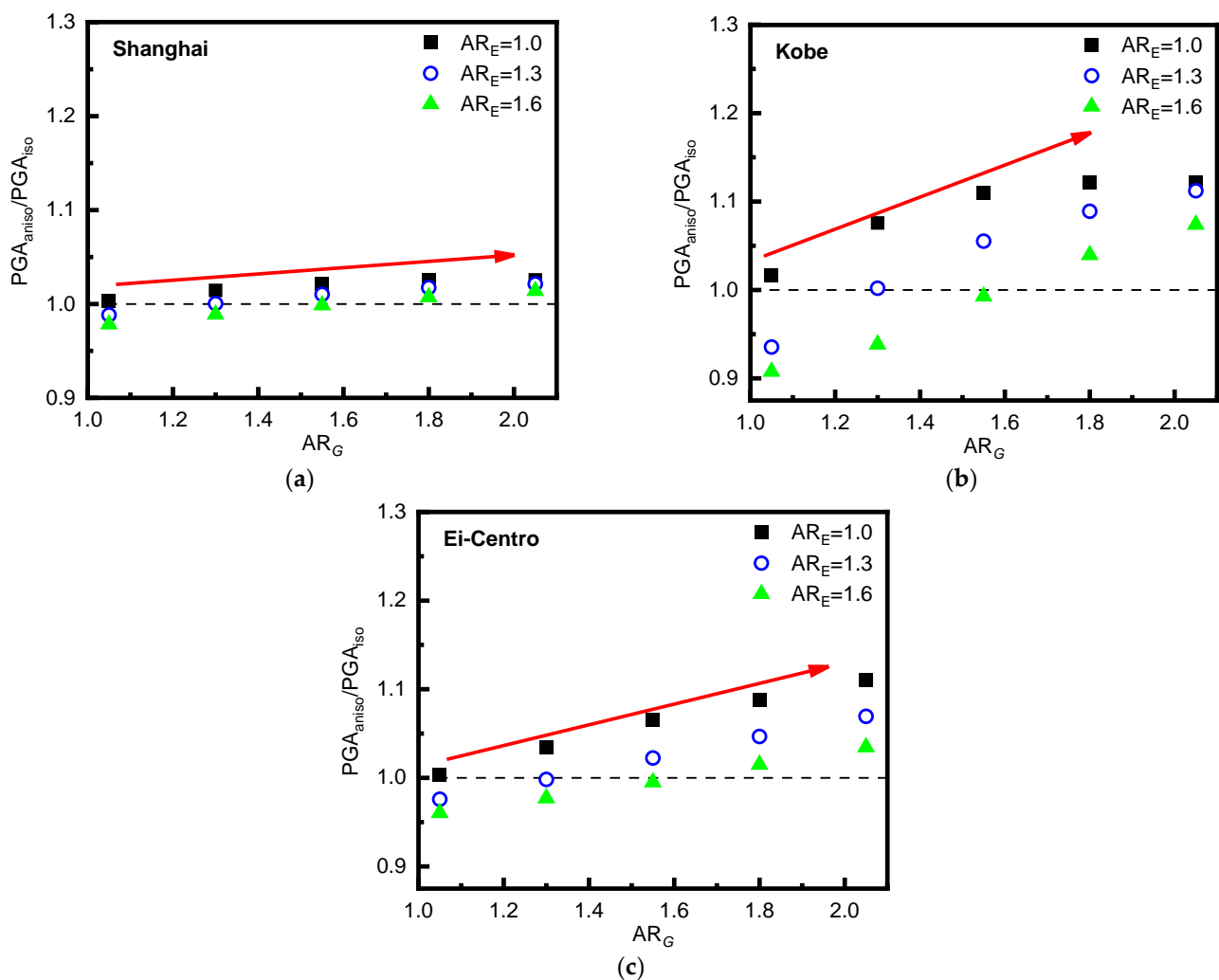
3.3. The Influence of Anisotropic Parameters

It should be noted that this study assumes a consistent relationship between $G_{vh} - \gamma$ and $G_{hh} - \gamma$. Different anisotropic parameter ($AR_E = 1.00, 1.30, 1.60$; $AR_G = 1.05, 1.30, 1.55, 1.80, 2.05$) were selected for a 30-meter-thick layer of soft soil with a shear wave velocity of 150 m/s. Detailed parameters are listed in Table 3.

Table 3. Example parameters.

Seismic Wave	AR_E	AR_G	Thickness (m)	V_s (m/s)	ρ (g/cm ³)
EI-Centro;	1.00;	1.05;	30	150	2
Shanghai;	1.30;	1.30;			
Kobe	1.60;	1.55;			
		1.80;			
		2.05;			

PGA_{aniso}/PGA_{iso} is the ratio between the peak ground acceleration obtained at an anisotropic site and that obtained at an isotropic site. Figure 4 shows that, with AR_E increasing, PGA_{aniso}/PGA_{iso} gradually decreases. Conversely, as AR_G increases, PGA has an obvious increase. Especially when inputting the Kobe wave, the PGA of anisotropic conditions exceeds that of isotropic conditions up to 14% with AR_G increasing. Consequently, it is considered that soil anisotropy is essential in analyzing site conditions for seismic response.

**Figure 4.** Normalized peak ground acceleration scatter plot: (a) Shanghai; (b) Kobe; (c) Ei-Centro.

To assess the impact of anisotropy on the seismic response, the dominant frequency of the seismic waves and the fundamental frequency of the site are further discussed

as listed in Table 4, where the fundamental frequency of the site is calculated using Equation (12) [53]:

$$f_g = \frac{1}{T_g} = V_{Si} / 4 \sum_{i=1}^n H_i \quad (12)$$

where the symbol “ f_g ” represents the fundamental frequency of the site; “ T_g ” refers to the site’s characteristic period; and the variable “ H_i ” denotes the thickness of individual soil layers, whereas “ V_{Si} ” represents the shear wave velocity specific to each respective soil layer.

Table 4. Site fundamental frequency and seismic wave dominant frequency.

Seismic Wave	Dominant Frequency of Seismic Wave (Hz)	f_g (Hz)
Shanghai	0.92	
Kobe	1.2	1.25
Ei-Centro	1.16	

As shown in Figure 4, the Ei-Centro and Kobe waves have significant influences on the PGA_{aniso} / PGA_{iso} , while the Shanghai wave has a relatively slight effect. From Table 4, compared with the dominant frequency of the Shanghai wave, those of the Kobe wave and Ei-Centro waves are closer to the fundamental frequency of the site. The waves with dominant frequencies closer to the fundamental frequencies of the sites may result in having a more significant effect in terms of anisotropy. Therefore, detailed investigations on the effects of the soil anisotropy on the seismic response of the Shanghai Yangshan Port site are conducted as an example.

4. Seismic Response of Shanghai Yangshan Port

4.1. Input Seismic Wave

The seismic characteristics of Yangshan Port are examined in this study through the analysis of artificial seismic wave data from Shanghai. According to the site classification method specified in the “Code for Seismic Design of Buildings” (GB 50011-2010) [54], the Yangshan Port area belongs to the fourth category of site. Based on the linear elastic soil layer, the ground acceleration time history is inverted to bedrock to obtain the bedrock acceleration time history [55].

4.2. Calculation Model and Parameters of Soil Layer

Most of the topsoil in Yangshan port is soft clay [56], and there is sand soil in the lower layer. Through the geological investigation, the site of Yangshan Port consists of four typical soil layers: clay layer, silty clay layer, muddy silty clay, and sand soil layer. According to Hou [57], the AR_E values for this area range from 1.6 to 2.40. Li [58] reported AR_C values ranging from 1.08 to 1.39 for Shanghai soil, while Ng [59] stated that the values were between 1.07 and 1.38. Detailed borehole data for the soil layers are provided in Table 5.

Table 5. Soil layer information of Yangshan port.

Number	Soil	Bottom Depth (m)	V_s (m/s)	ρ (g/cm ³)
1	Muddy silty clay	17.6	140	
2	Clay	21.6	180	1.8
3	Silty clay	31.2	230	
4	Sand	43.2	290	2

Resonance column and cyclic triaxial tests were conducted to obtain $G_{norm} - \gamma$ and $D - \gamma$ curves for clay, silty clay layer, muddy silty clay, and sand. The design confining pressures are 150 kPa, 200 kPa, and 250 kPa for clay, silty clay layer, and muddy silty clay.

The design confining pressures are 200 kPa, 250 kPa, and 300 kPa for sand. Figure 5 shows the details of the cyclic triaxial test and the resonant column test. The experimental results pertaining to silty clay are specifically analyzed in this study. Figure 6 illustrates the S-wave output signals of the bending element in the silty clay specimen subjected to a confining pressure of 150 kPa across different input frequencies. Furthermore, the G_0 value derived from the bending element tests is approximately 1.1 to 1.2 times greater than the results obtained from the resonant column tests, which aligns with the outcomes reported by Yang et al. [60] and Gu et al. [61,62]. The reason behind this is that the results of the bending element tests specifically relate to the localized stiffness of the shear wave propagation path, while the resonant column offer insights into the overall stiffness characteristics of the specimens [60–62]. This confirms the accuracy of the resonant column test. Simultaneously, Yang et al. [60], Gu et al. [61,62], and Youn et al. [63] propose to determine G_0 based on the resonant column test.

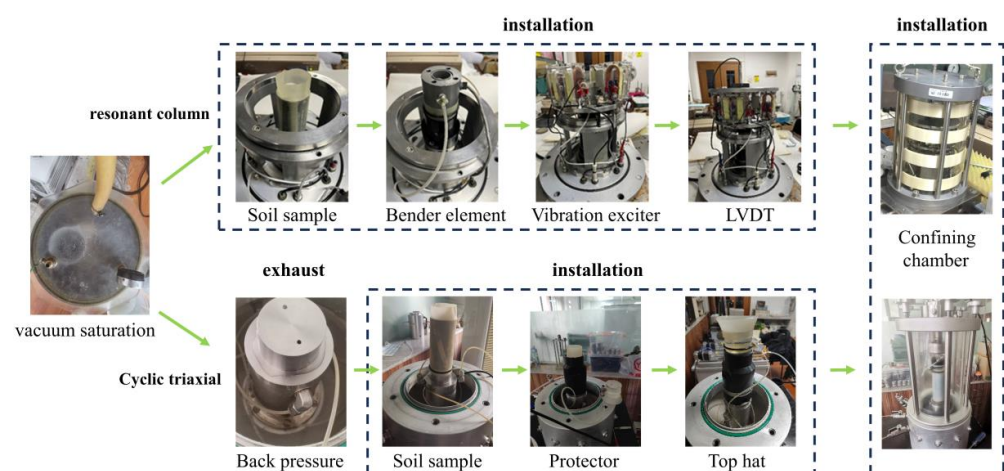


Figure 5. Cyclic triaxial test and resonant column test details.

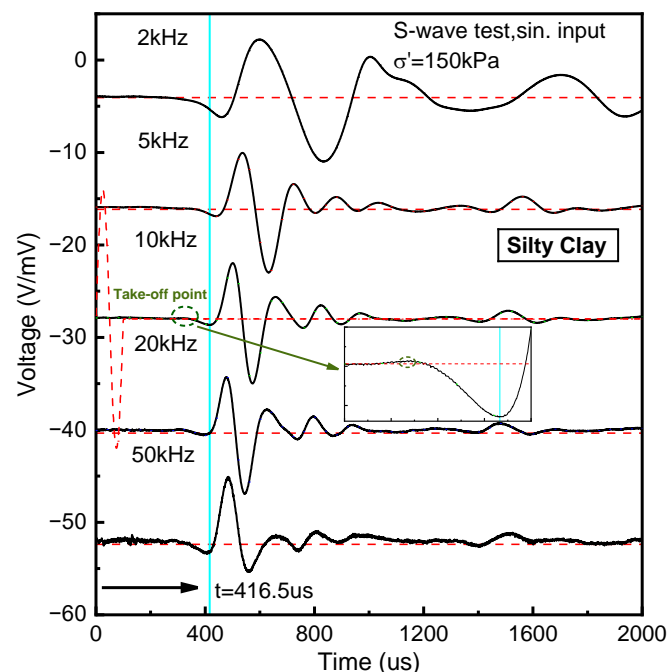


Figure 6. BE S-wave signals in silty clay specimen.

The cyclic triaxial experiments were performed employing strain control. To mitigate the influence of cyclic loading on subsequent tests, the number of cycles for each loading

stage was limited to six. Figure 7 depicts the outcomes of the cyclic triaxial tests conducted on the silty clay. The modulus degrades as the strain increases, while it amplifies with the elevated confining pressure. Through fitting analysis, we obtained the $G_{norm} - \gamma$ and $D - \gamma$ curves for clay in the Yangshan Port site. Figure 8 depicts the curve of best fit for the silty clay specimen. For the other soil layers, the model parameters calibrated from the resonance column and the cyclic triaxial tests are also provided in Table 6.

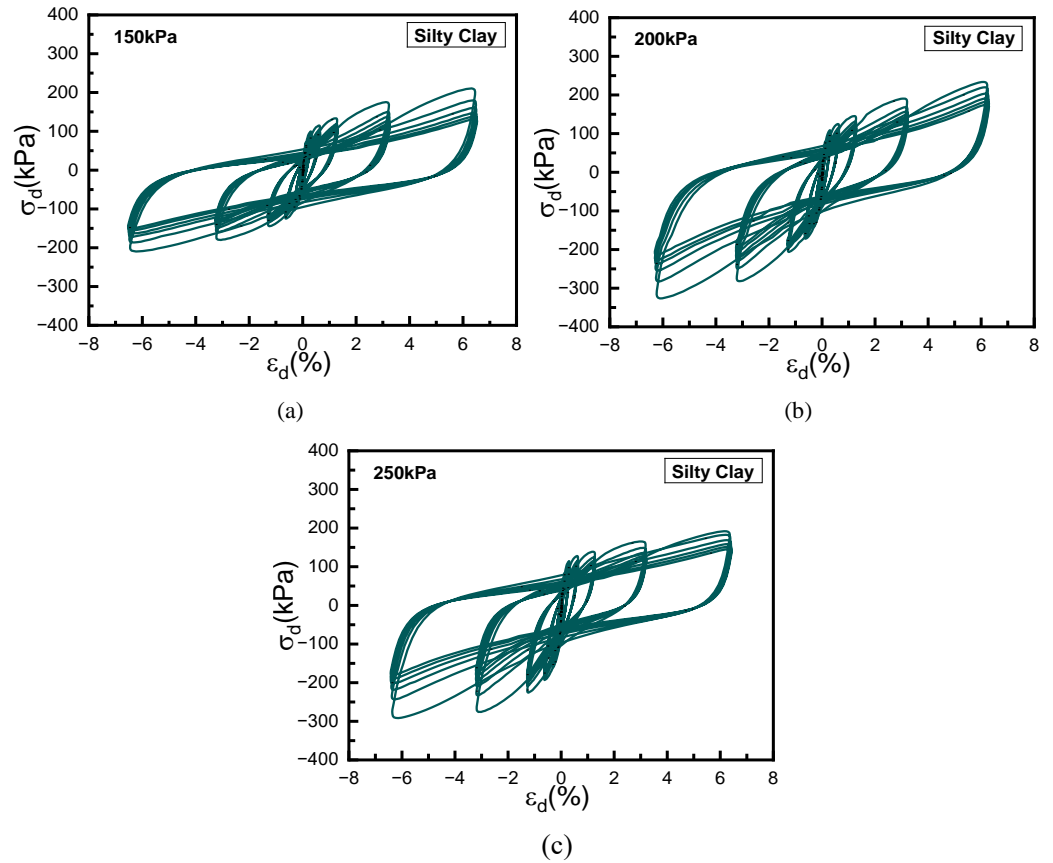


Figure 7. Partial results of cyclic triaxial testing (silty clay): (a) 150 kpa; (b) 200 kpa; (c) 250 kpa.

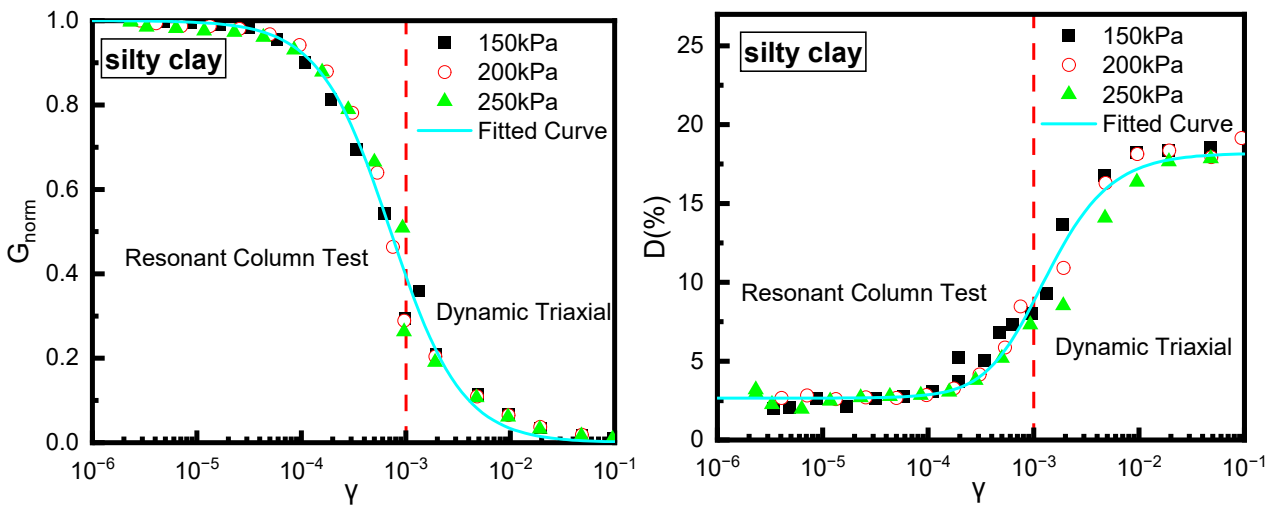


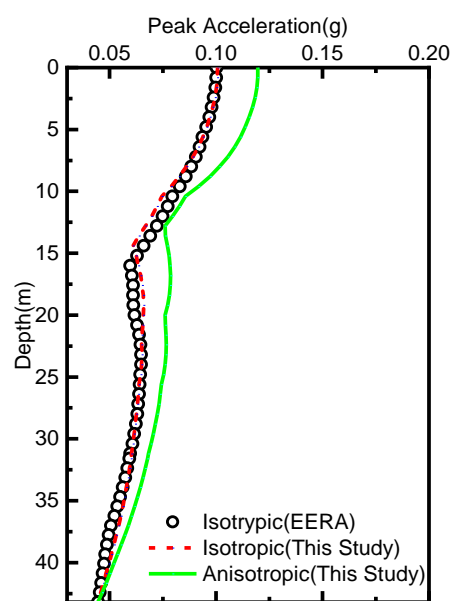
Figure 8. (a) $G_{norm} - \gamma$; (b) $D - \gamma$.

Table 6. The soil parameters of the Yangshan Port site.

Soil	$\gamma_\gamma (10^{-4})$	α	K_1	K_2	K_3
Clay	8.1	1.28	0.16	−0.32	0.19
Silty Clay	7.17	1.27	0.14	−0.29	0.18
Muddy silty Clay	7.32	1.31	0.10	−0.26	0.18
sand	6.09	1.07	0.12	−0.26	0.16

4.3. Results

Taking into account the previous discussion regarding the suppressive effect of AR_E and the enhancing effect of AR_G on PGA performance, we initially selected a value of 1.6 for AR_E and a value of 1.4 for AR_G to simulate the unfavorable conditions. In this case, study, the Shanghai wave is adjusted to have peak ground acceleration of 0.1 g. Figures 9 and 10 show the changes in peak acceleration along the depth and the ground peak acceleration spectrum, respectively. It is evident that when the proposed calculation model reduces to the isotropic scenario, it aligns well with the results obtained from EERA. However, when considering soil anisotropy, the PGA increases by 19.70%; the peak value of the ground response spectrum undergoes a significant increase of 28.82% at 1 Hz.

**Figure 9.** Peak acceleration along depth.

In order to discuss the influence of anisotropy on the ground acceleration frequency, the ground motion response of the Ei-Centro waves and Kobe waves input at Yangshan port is calculated. The result can be seen in Figure 10. It can be found that anisotropy has little influence on the frequency position of the ground Fourier acceleration spectrum peak.

To further explore the design response spectrum of Yangshan Port, the ground motion responses of the site under different seismic intensities (0.1 g, 0.15 g, 0.2 g, 0.25 g, 0.3 g) are studied. Based on the 5% damped ground acceleration response spectrum of different intensities, the least squares method by Andreotti [64] et al. was used to calibrate the design response spectrum. The shape function of the design response spectrum by Chinese code “GB 51247-2018” is as follows [65]:

$$\beta(T) = \begin{cases} 1 + (\beta_{\max} - 1) \frac{T}{T_0} & 0 \leq T \leq T_0 \\ \beta_{\max} & T_0 \leq T \leq T_g \\ \beta_{\max} \left(\frac{T_g}{T} \right)^\chi & T_g \leq T \leq T_m \end{cases} \quad (13)$$

where T_0 is the period associated with the initial inflection point, established at 0.1 s. T_g signifies the characteristic period. Since this study focuses on a certain soil layer in Yangshan Port, the characteristic period (T_g) can be calculated according to Equation (12), which is 0.92 s. T_m is the cutoff period, χ represents the attenuation index, and β_{max} denotes the plateau value.

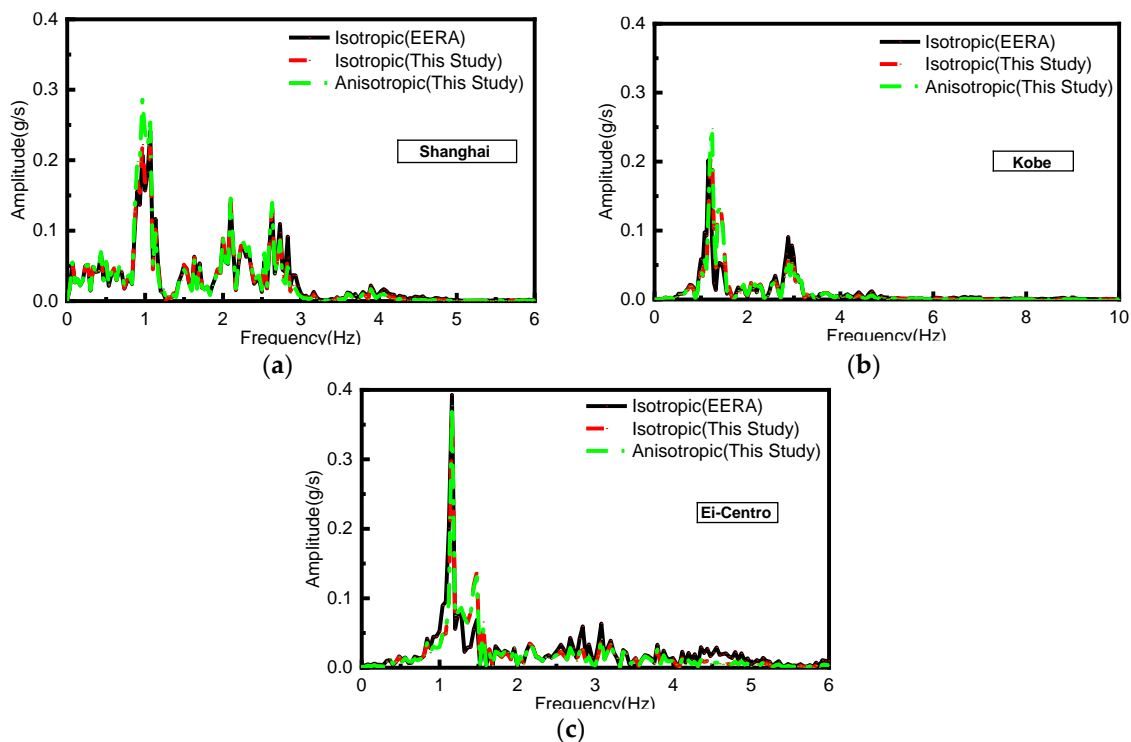


Figure 10. Ground Fourier acceleration spectrum: (a) Shanghai; (b) Kobe; (c) Ei-Centro.

As well as that given in Equation (13) (termed as “Shape Function One”), another two typical commonly used shape functions shown in Figure 11 are also collected for calibrating the design response spectrum for Yangshan Port. Shape Function Two was provided by Deoda and Adhikary (2020) [66], where T_D is defined as the value defining the beginning of the constant displacement response range of the spectrum. Shape Function Three is employed by both NZS 1170.5 [67] and Eurocode 8 [51].

The gray lines in Figure 11 are the ground response spectrums at different intensities with consideration of soil anisotropy. The upper and lower bounds of the gray area are the 16th to 84th percentiles, respectively, showing the region with a probability range of 16% to 84% for the occurrence of seismic events. The red line represents the average of the response spectrum curve. Utilizing Shape Function One, the 5% damped design response spectrum for Yangshan Port is calibrated and represented by the blue line. The design response spectrums based on Shape Function Two and Three are depicted as the magenta and orange lines, respectively.

For Shape Function One suggested by GB 51247-2018, the plateau value (β) is 2.97, and the attenuation index (χ) is 0.5. The Pearson correlation coefficient (r value) is 0.63. Additionally, utilizing Shape Function Two results in a plateau value (β) of 3.00 and an attenuation index (χ) of 0.5. This yields a Pearson correlation coefficient (r value) of 0.57. Similarly, when employing Shape Function Three, the plateau value (β) is 3.00, while the attenuation index (χ) is 0.5, with a significantly higher Pearson correlation coefficient (r value) of 0.71. Three shape functions provide a similar plateau value (β), but Shape Function Three exhibits a better overall fitting performance.

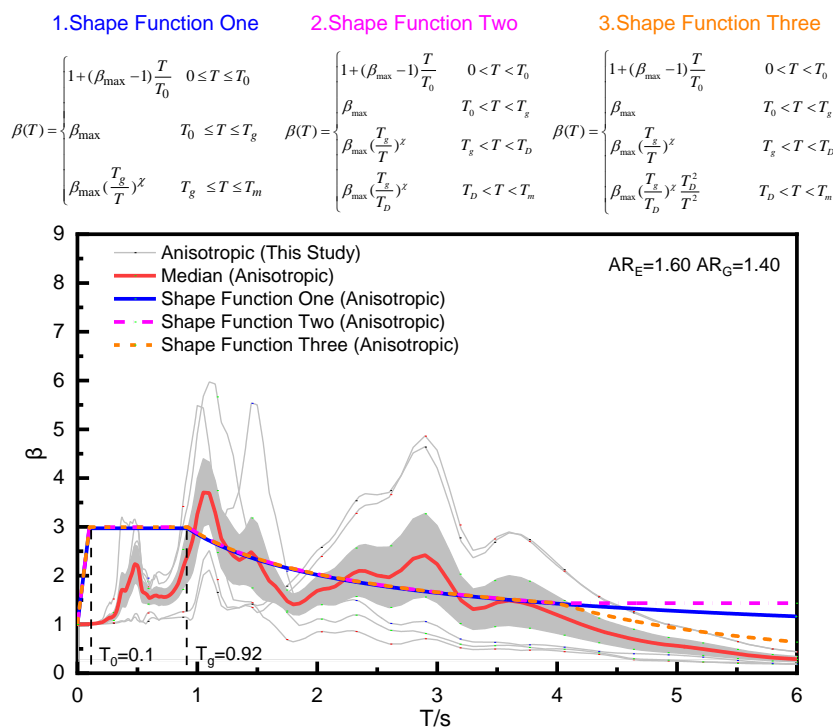


Figure 11. The 5% damped design response spectrum for Yangshan Port ($AR_E = 1.60, AR_G = 1.40$).

To further investigate the influence of anisotropy on ground response spectra, a series of cross-parameter studies were conducted focusing on anisotropy-related parameters (elastic modulus ratio $AR_E = 1.60, 2.00, 2.40$; shear modulus ratio $AR_G = 1.10, 1.25, 1.40$), resulting in a total of nine combinations. Following the method illustrated in Figure 11, Figure 12 presents nine average response spectrum curves. Utilizing the mean values of these spectrums, the root mean square error (RMSE) across the entire period range for the nine response spectrum curves was calculated and is depicted by the gray line in Figure 12. It is observed that the maximum RMSE among the nine response spectrum curves reaches 34.5% at lower frequencies.

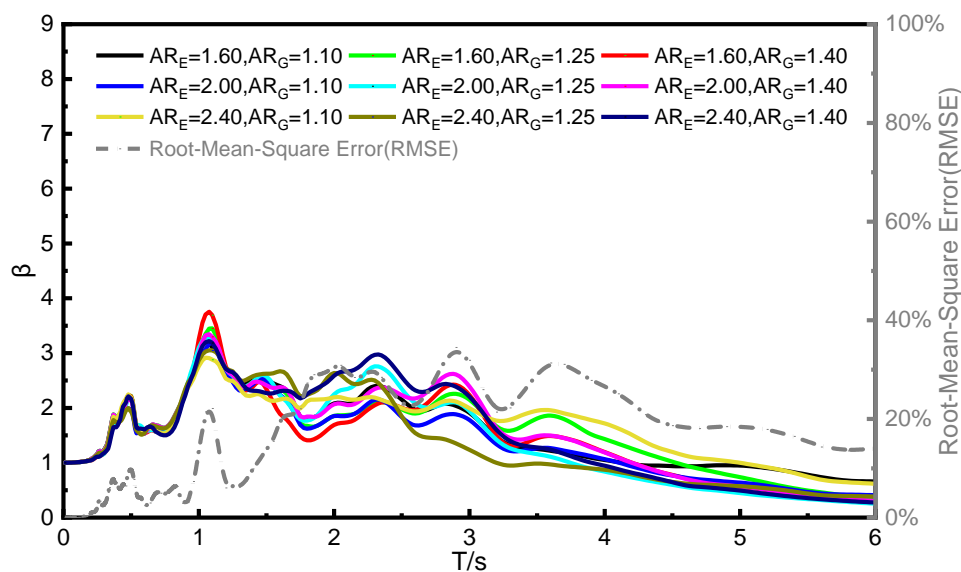


Figure 12. The 5% damped design response spectrum for Yangshan Port (different anisotropic parameters).

Finally, the proposed 5% damped standard design response spectrum for Yangshan Port has been developed from the previously described nine combinations of anisotropic parameters and five seismic intensity levels. The design response spectrum for the anisotropic site is refined using Shape Function Three, which is depicted as an orange line in Figure 13. This calibration involves a plateau value (β) of 3.00 and an attenuation index (χ) of 0.50. When compared to the isotropic spectrum, the anisotropic spectrum demonstrates a notably elevated design response spectrum. Factoring in anisotropy has led to an increase of 18% in the plateau value (β) for the standard design response spectrum. Consequently, utilizing the isotropic design response spectrum for the seismic design of structures at Shanghai Yangshan Port may result in dangerous results.

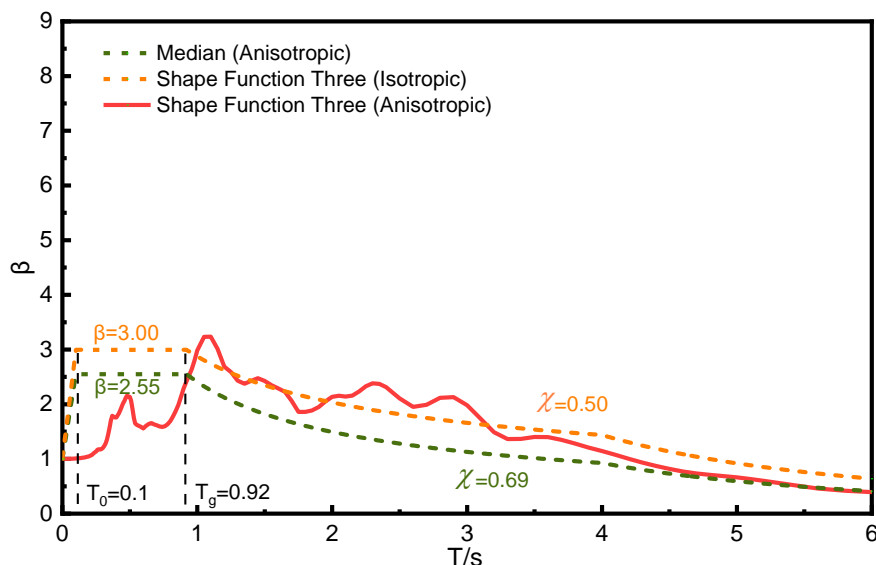


Figure 13. Proposed 5% damped standard design response spectrum for Yangshan Port.

Figure 14 illustrates the application of the response spectrum for a single-degree-of-freedom model. When utilizing the response spectrum, two key aspects must be contemplated. Firstly, the fundamental frequency ($f = 2\pi\sqrt{m/k}$) is derived from the concentration of mass and lateral stiffness. Secondly, the design base shear is computed through $F = m\beta \times PGA$.

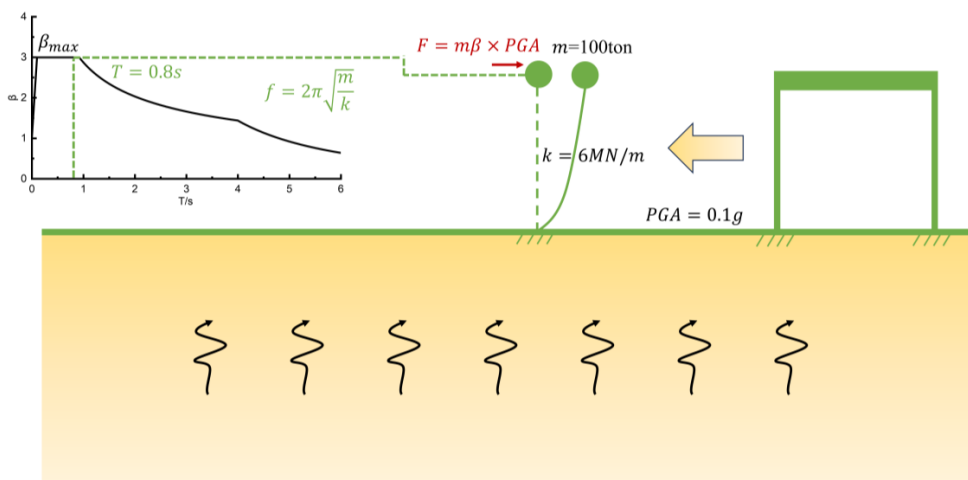


Figure 14. Application of response spectrum for single-degree-of-freedom systems.

For instance, let us consider a single-story frame with a total seismic weight of 980 kN and a total column lateral stiffness k of 6 MN/m. The structure has a damping ratio of 5%.

The basic acceleration (PGA) by design is 0.1 g. For the conventional response spectrum, the design base shear amounts to 250 kN. However, when the response spectrum is applied with consideration of anisotropy, the design base shear amounts to 294 kN, marking an increase of 18%.

5. Conclusions

This study establishes an equivalent linear ground motion model for anisotropic sites to analyze the ground motion response characteristics for layered soils with various anisotropy parameters. Further investigations were conducted to study the ground motion response features of anisotropic sites when subjected to different seismic wave inputs. It was found that the anisotropy ratios for the shear modulus (AR_G) have a promoting effect on the peak ground acceleration (PGA), while the anisotropic ratio of undrained Young's modulus (AR_E) has an inhibitory effect on peak ground acceleration (PGA) in the site earthquake response problem. The impact of anisotropy on the ground motion of the site becomes more significant when seismic waves have dominant frequencies closer to the fundamental frequencies of the sites. In the ground motion response problem, anisotropy cannot be ignored when the dominant frequencies of the seismic waves are closer to the fundamental frequencies of the sites.

This study further takes the Yangshan Port site as an example to calibrate the seismic motion parameters ($G - \gamma$ and $D - \gamma$) of the Yangshan Port soil layer based on cyclic triaxial tests and resonant column tests. The results show that the combination of the resonant column test and cyclic triaxial test can better describe the dynamic characteristics of soil from small strains ($10^{-6} \sim 10^{-3}$) to large strains ($10^{-3} \sim 10^{-1}$). Based on the calibrated dynamic parameters, the ground motion characteristics of the anisotropic site of Yangshan Port were studied. It was found that the consideration of site anisotropy leads to significant increases in both the peak ground acceleration (PGA) and the peak ground Fourier acceleration spectrum for the Yangshan Port site. Anisotropy has little influence on the frequency position of the ground Fourier acceleration spectrum peak. The frequency region where the amplitude of the ground Fourier acceleration spectrum increases significantly is close to the site fundamental frequency (1 Hz). This demonstrates that site anisotropy can potentially lead to a severe underestimation of the acceleration response in regions proximate to the site's fundamental frequency.

A series of cross-parameter studies regarding anisotropic parameters were also conducted to investigate the influence of anisotropy on ground response spectra. When taking site anisotropy into account, the calibrated design response spectrum plateau value (β) is 3.00. Conversely, when anisotropy is not considered, the calibrated design response spectrum plateau value (β) stands at 2.55. The design response spectrum calibrated for an anisotropic site surpasses that for an isotropic site. Thus, when performing the seismic design of buildings, utilizing the design response spectrum derived from isotropic site ground motion response calibration might present higher risks.

Author Contributions: Conceptualization, Z.C. and J.Y.; Methodology, Y.X. and J.Y.; Software, Y.X.; Resources, Z.C.; Writing – original draft, Y.X.; Writing – review & editing, J.Y.; Visualization, Y.X.; Supervision, Z.C. and J.Y.; Funding acquisition, Z.C. and J.Y. All authors have read and agreed to the published version of the manuscript.

Funding: This work was supported by the National Key Research and Development Program of China (No. 2021YFB2600700) and the Natural Science Foundation of Shanghai (No. 23ZR1468500).

Data Availability Statement: Data are available upon request.

Conflicts of Interest: The authors declare no conflict of interest.

References

1. Tong, X.; Hong, Z.; Liu, S.; Zhang, X.; Xie, H.; Li, Z.; Bao, F. Building-damage detection using pre-and post-seismic high-resolution satellite stereo imagery: A case study of the May 2008 Wenchuan earthquake. *ISPRS J. Photogramm. Remote Sens.* **2012**, *68*, 13–27. [CrossRef]
2. Zhang, M.; Jin, Y. Building damage in Dujiangyan during Wenchuan earthquake. *Earthq. Eng. Eng. Vib.* **2008**, *7*, 263–269. [CrossRef]
3. An, X.; Shawky, A.A.; Maekawa, K. The collapse mechanism of a subway station during the Great Hanshin earthquake. *Cem. Concr. Compos.* **1997**, *19*, 241–257. [CrossRef]
4. Kelam, A.A.; Karimzadeh, S.; Yousefibavil, K.; Akgün, H.; Askan, A.; Erberik, M.A.; Ciftci, H. An evaluation of seismic hazard and potential damage in Gaziantep, Turkey using site specific models for sources, velocity structure and building stock. *Soil Dyn. Earthq. Eng.* **2022**, *154*, 107129. [CrossRef]
5. Polat, O.; Çeken, U. Investigation of the local soil effects at the new strong-motion array (MATNet) in Hatay-K. Maras Region, Turkey. In Proceedings of the AGU Fall Meeting, San Francisco, CA, USA, 15–19 December 2014. abstract S13F–07.
6. Wardman, J.; Officer, C.C. The 2023 Kahramanmaraş Earthquake Sequence: A Counterfactual Contemplation—On 6 February 2023 a Magnitude Mw7. 8 and Mw7. 6 Earthquake Doublet Occurred in the East Anatolian Fault Zone Resulting in Catastrophic Destruction and Loss of Life in Southeast-Central Turkey and Northern Syria. Knowing What We Know Now, How Might the Events Have Played Out Differently? Available online: <https://www.maxinfo.io/blog/the-2023-kahramanmaras-earthquake-sequence-a-counterfactual-perspective> (accessed on 1 December 2023).
7. Askan, A.; Gülerce, Z.; Roumelioti, Z.; Sotiriadis, D.; Melis, N.S.; Altindal, A.; Margaris, B. The Samos Island (Aegean Sea) M7. 0 earthquake: Analysis and engineering implications of strong motion data. *Bull. Earthq. Eng.* **2022**, *20*, 7737–7762. [CrossRef]
8. Daraei, A.; Hama Ali, H.F.; Qader, D.N.; Zare, S. Seismic retrofitting of rubble masonry tunnel: Evaluation of steel fiber shotcrete or inner concrete lining alternatives. *Arab. J. Geosci.* **2022**, *15*, 1074. [CrossRef]
9. Preciado, A.; Santos, J.C.; Silva, C.; Ramírez-Gaytán, A.; Falcon, J.M. Seismic damage and retrofitting identification in unreinforced masonry Churches and bell towers by the september 19, 2017 (Mw = 7.1) Puebla-Morelos earthquake. *Eng. Fail. Anal.* **2020**, *118*, 104924. [CrossRef]
10. Aaqib, M.; Park, D.; Adeel, M.B.; Hashash, Y.M.; Ilhan, O. Simulation-based site amplification model for shallow bedrock sites in Korea. *Earthq. Spectra* **2021**, *37*, 1900–1930. [CrossRef]
11. Adeel, M.B.; Nizamani, Z.A.; Aaqib, M.; Khan, S.; Rehman, J.U.; Bhusal, B.; Park, D. Estimation of V S30 using shallow depth time-averaged shear wave velocity of Rawalpindi–Islamabad, Pakistan. *Geomat. Nat. Hazards Risk* **2023**, *14*, 1–21. [CrossRef]
12. Bhusal, B.; Aaqib, M.; Paudel, S.; Parajuli, H.R. Site specific seismic hazard analysis of monumental site Dharahara, Kathmandu, Nepal. *Geomat. Nat. Hazards Risk* **2022**, *13*, 2674–2696. [CrossRef]
13. Joyner, M.D.; Gardner, C.; Puentes, B.; Sasani, M. Resilience-Based seismic design of buildings through multiobjective optimization. *Eng. Struct.* **2021**, *246*, 113024. [CrossRef]
14. Morandi, P.; Butenweg, C.; Breis, K.; Beyer, K.; Magenes, G. Latest findings on the behaviour factor q for the seismic design of URM buildings. *Bull. Earthq. Eng.* **2022**, *20*, 5797–5848. [CrossRef]
15. Leyva, H.; Bojórquez, J.; Bojórquez, E.; Reyes-Salazar, A.; Carrillo, J.; López-Almansa, F. Multi-objective seismic design of BRBs-reinforced concrete buildings using genetic algorithms. *Struct. Multidiscip. Optim.* **2021**, *64*, 2097–2112. [CrossRef]
16. Jiang, J.; El Nggar, H.M.; Xu, C.; Zhong, Z.; Du, X. Effect of ground motion characteristics on seismic fragility of subway station. *Soil Dyn. Earthq. Eng.* **2021**, *143*, 106618. [CrossRef]
17. Mo, T.; Wu, Q.; Li, D.Q.; Du, W. Influence of ground motion characteristics (velocity pulse and duration) on the pile responses in liquefiable soil deposits. *Soil Dyn. Earthq. Eng.* **2022**, *159*, 107330. [CrossRef]
18. Zhang, X.; Tang, L.; Ling, X.; Chan, A.H.C.; Lu, J. Using peak ground velocity to characterize the response of soil-pile system in liquefying ground. *Eng. Geol.* **2018**, *240*, 62–73. [CrossRef]
19. Wang, Z.Z.; Zhang, J.; Huang, H. Interpreting random fields through the U-Net architecture for failure mechanism and deformation predictions of geosystems. *Geosci. Front.* **2024**, *15*, 101720. [CrossRef]
20. Dammala, P.K.; Kumar, S.S.; Krishna, A.M.; Bhattacharya, S. Dynamic soil properties and liquefaction potential of northeast Indian soil for non-linear effective stress analysis. *Bull. Earthq. Eng.* **2019**, *17*, 2899–2933. [CrossRef]
21. Markham, C.S.; Bray, J.D.; Macedo, J.; Luque, R. Evaluating nonlinear effective stress site response analyses using records from the Canterbury earthquake sequence. *Soil Dyn. Earthq. Eng.* **2016**, *82*, 84–98. [CrossRef]
22. Chen, G.; Wang, Y.; Zhao, D.; Zhao, K.; Yang, J. A new effective stress method for nonlinear site response analyses. *Earthq. Eng. Struct. Dyn.* **2021**, *50*, 1595–1611. [CrossRef]
23. Li, Z.; Liu, H. An isotropic-kinematic hardening model for cyclic shakedown and ratcheting of sand. *Soil Dyn. Earthq. Eng.* **2020**, *138*, 106329. [CrossRef]
24. Elia, G.; Rouainia, M. Investigating the cyclic behaviour of clays using a kinematic hardening soil model. *Soil Dyn. Earthq. Eng.* **2016**, *88*, 399–411. [CrossRef]
25. Moghadam, S.I.; Taheri, E.; Ahmadi, M.; Ghoreishian Amiri, S.A. Unified bounding surface model for monotonic and cyclic behaviour of clay and sand. *Acta Geotech.* **2022**, *17*, 4359–4375. [CrossRef]
26. Cheng, X.; Du, X.; Lu, D.; Ma, C.; Wang, P. A simple single bounding surface model for undrained cyclic behaviours of saturated clays and its numerical implementation. *Soil Dyn. Earthq. Eng.* **2020**, *139*, 106389. [CrossRef]

27. Shi, Z.; Huang, M. Intergranular-strain elastic model for recent stress history effects on clay. *Comput. Geotech.* **2020**, *118*, 103316. [[CrossRef](#)]
28. Huang, X.W.; Guo, J.; Li, K.Q.; Wang, Z.Z.; Wang, W. Predicting the thermal conductivity of unsaturated soils considering wetting behavior: A meso-scale study. *Int. J. Heat Mass Transf.* **2023**, *204*, 123853. [[CrossRef](#)]
29. Elbadawy, M.A.; Zhou, Y.G.; Liu, K. A modified pressure dependent multi-yield surface model for simulation of LEAP-Asia-2019 centrifuge experiments. *Soil Dyn. Earthq. Eng.* **2022**, *154*, 107135. [[CrossRef](#)]
30. Mroz, Z. On the description of anisotropic workhardening. *J. Mech. Phys. Solids* **1967**, *15*, 163–175. [[CrossRef](#)]
31. Hardin, B.O.; Drnevich, V.P. Shear modulus and damping in soils: Measurement and parameter effects (terzaghi lecture). *J. Soil Mech. Found. Div.* **1972**, *98*, 603–624. [[CrossRef](#)]
32. Hardin, B.O.; Drnevich, V.P. Shear modulus and damping in soils: Design equations and curves. *J. Soil Mech. Found. Div.* **1972**, *98*, 667–692. [[CrossRef](#)]
33. Schnabel, P.B. *SHAKE, a Computer Program for Earthquake Response Analysis of Horizontally Layered Sites*; Report No. EERC 72-12; University of California: Berkeley, CA, USA, 1972.
34. Wang, J.P.; Xu, Y. A non-stationary earthquake probability assessment with the Mohr–Coulomb failure criterion. *Nat. Hazards Earth Syst. Sci.* **2015**, *15*, 2401–2412. [[CrossRef](#)]
35. Luo, C.; Yang, X.; Zhan, C.; Jin, X.; Ding, Z. Nonlinear 3D finite element analysis of soil–pile–structure interaction system subjected to horizontal earthquake excitation. *Soil Dyn. Earthq. Eng.* **2016**, *84*, 145–156. [[CrossRef](#)]
36. Idriss, I.M.; Sun, J.I. A Computer program for conducting equivalent linear seismic response analysis of horizontally layered soil deposits. In *Users Manual for SHAKE91*; University of California, Berkeley: Berkeley, CA, USA, 1992.
37. Zhang, R.; Wu, C.; Goh, A.T.; Böhlke, T.; Zhang, W. Estimation of diaphragm wall deflections for deep braced excavation in anisotropic clays using ensemble learning. *Geosci. Front.* **2021**, *12*, 365–373. [[CrossRef](#)]
38. Zhang, R.; Li, Y.; Goh, A.T.; Zhang, W.; Chen, Z. Analysis of ground surface settlement in anisotropic clays using extreme gradient boosting and random forest regression models. *J. Rock Mech. Geotech. Eng.* **2021**, *13*, 1478–1484. [[CrossRef](#)]
39. Teng, F. A Simplified Expression for Ground Movements Induced by Excavations in Soft Clay. In *Proceedings of the 2nd International Symposium on Asia Urban GeoEngineering, Changsha, China, 24–27 November 2017*; Springer: Singapore, 2018; pp. 93–115.
40. Wei, F.; Wang, H.; Zeng, G.; Jiang, M. Seepage flow around twin circular tunnels in anisotropic ground revealed by an analytical solution. *Undergr. Space* **2023**, *10*, 1–14. [[CrossRef](#)]
41. Soe, T.E.E.; Ukritchon, B. Three-dimensional undrained face stability of circular tunnels in non-homogeneous and anisotropic clays. *Comput. Geotech.* **2023**, *159*, 105422. [[CrossRef](#)]
42. Zhang, W.; Li, Y.; Wu, C.; Li, H.; Goh, A.T.C.; Liu, H. Prediction of lining response for twin tunnels constructed in anisotropic clay using machine learning techniques. *Undergr. Space* **2022**, *7*, 122–133. [[CrossRef](#)]
43. Perić, D.; Tran, T.V.; Miletic, M. Effects of soil anisotropy on a soil structure interaction in a heat exchanger pile. *Comput. Geotech.* **2017**, *86*, 193–202. [[CrossRef](#)]
44. Ai, Z.Y.; Ye, J.M.; Zhao, Y.Z. The performance analysis of energy piles in cross-anisotropic soils. *Energy* **2022**, *255*, 124549. [[CrossRef](#)]
45. Ai, Z.Y.; Ye, J.M. Thermo-mechanical analysis of pipe energy piles in layered cross-isotropic soils. *Energy* **2023**, *277*, 127757. [[CrossRef](#)]
46. Bentil, O.T.; Zhou, C.; Zhang, J.; Liu, K.K. Cross-anisotropic stiffness characteristics of a compacted lateritic clay from very small to large strains. *Can. Geotech. J.* **2023**. [[CrossRef](#)]
47. Stokoe, K.H.; Darendeli, M.B.; Andrus, R.D.; Brown, L.T. Dynamic soil properties: Laboratory, field and correlation studies. In *Earthquake Geotechnical Engineering*; CRC Press: Boca Raton, FL, USA, 1999; pp. 811–845.
48. Zhang, M.; Liao, W.M.; Wang, Z.J. Statistical analysis of the relationship between dynamic shear modulus ratio and damping ratio and shear strain of cohesive soil. *Earthq. Eng. Eng. Vib.* **2013**, *33*, 256–262.
49. Nishimura, S. Cross-anisotropic deformation characteristics of natural sedimentary clays. *Géotechnique* **2014**, *64*, 981–996. [[CrossRef](#)]
50. Teng, F.C.; Ou, C.Y.; Hsieh, P.G. Measurements and numerical simulations of inherent stiffness anisotropy in soft Taipei clay. *J. Geotech. Geoenviron. Eng.* **2014**, *140*, 237–250. [[CrossRef](#)]
51. *EN 1998-5; Eurocode 8: Design of Structures for Earthquake*. CEN (European Committee for Standardization): Brussels, Belgium, 2004.
52. Seed, H.B. *Soil Moduli and Damping Factors for Dynamic Response Analyses*; Report EERC 70-10; University of California: Berkeley, CA, USA, 1970.
53. Forte, G.; Chioccarelli, E.; De Falco, M.; Cito, P.; Santo, A.; Iervolino, I. Seismic soil classification of Italy based on surface geology and shear-wave velocity measurements. *Soil Dyn. Earthq. Eng.* **2019**, *122*, 79–93. [[CrossRef](#)]
54. *GB 50011-2010; Code for Seismic Design of Buildings*. China Architecture Building Press: Beijing, China, 2010. (In Chinese)
55. Dong, F.F.; Chen, G.X.; Jin, D.D. Comparison of one-dimensional equivalent linear and two-dimensional nonlinear analysis of seismic effect characteristics in Quanzhou Basin. *J. Disaster Prev. Mitig. Eng.* **2014**, *34*, 154–160.
56. Zhang, J.Z.; Huang, H.W.; Zhang, D.M.; Phoon, K.K. Experimental study of the coupling effect on segmental shield tunnel lining under surcharge loading and excavation unloading. *Tunn. Undergr. Space Technol.* **2023**, *140*, 105199. [[CrossRef](#)]

57. Hou, Y.M.; Wang, J.H.; Zhang, L.L. Finite-element modeling of a complex deep excavation in Shanghai. *Acta Geotech.* **2009**, *4*, 7–16. [[CrossRef](#)]
58. Li, Q.; Ng, C.W.W.; Liu, G.B. Determination of small-strain stiffness of Shanghai clay on prismatic soil specimen. *Can. Geotech. J.* **2012**, *49*, 986–993. [[CrossRef](#)]
59. Ng, C.W.W.; Li, Q.; Liu, G.B. Experimental study on the measurement of anisotropic shear modulus of undisturbed Shanghai soft clay using bending elements. *Chin. J. Geotech. Eng.* **2013**, *35*, 150–156.
60. Yang, J.; Liu, X. Shear wave velocity and stiffness of sand: The role of non-plastic fines. *Géotechnique* **2016**, *66*, 500–514. [[CrossRef](#)]
61. Gu, X.; Yang, J.; Huang, M. Laboratory measurements of small strain properties of dry sands by bender element. *Soils Found.* **2013**, *53*, 735–745. [[CrossRef](#)]
62. Gu, X.Q.; Yang, J.; Huang, M.S.; Gao, G.Y. Bending element, resonant column and cyclic torsional shear tests for the determination of shear modulus of sand. *Chin. J. Geotech. Eng.* **2016**, *38*, 740–746.
63. Youn, J.U.; Choo, Y.W.; Kim, D.S. Measurement of small-strain shear modulus G_{max} of dry and saturated sands by bender element, resonant column, and torsional shear tests. *Can. Geotech. J.* **2008**, *45*, 1426–1438. [[CrossRef](#)]
64. Andreotti, G.; Famà, A.; Lai, C.G. Hazard-dependent soil factors for site-specific elastic acceleration response spectra of Italian and European seismic building codes. *Bull. Earthq. Eng.* **2018**, *16*, 5769–5800. [[CrossRef](#)]
65. *GB 51247-2018*; Standard for Seismic Design of Hydraulic Structures. China Architecture Building Press: Beijing, China, 2018. (In Chinese)
66. Deoda, V.R.; Adhikary, S. A preliminary proposal towards the revision of Indian seismic code considering site classification scheme, amplification factors and response spectra. *Bull. Earthq. Eng.* **2020**, *18*, 2843–2889. [[CrossRef](#)]
67. *NZS 1170.5*; Structural Design Actions, Part 5: Earthquake Actions. Standards New Zealand: Wellington, New Zealand, 2004.

Disclaimer/Publisher's Note: The statements, opinions and data contained in all publications are solely those of the individual author(s) and contributor(s) and not of MDPI and/or the editor(s). MDPI and/or the editor(s) disclaim responsibility for any injury to people or property resulting from any ideas, methods, instructions or products referred to in the content.